Flow Turbulence Combust (2014) 93:723–739
DOI 10.1007/s10494-014-9568-y

Measurement of Three-Dimensional Temperature Field of Flickering Premixed Flame with and without Coflow

N. Fujisawa · J. Yamada · T. Yamagata

Received: 21 April 2014 / Accepted: 4 September 2014 / Published online: 20 September 2014

Abstract The three-dimensional (3D) temperature field of the flickering flame with and without coflow can be measured using the flame reaction technique combined with tomographic reconstruction. This combined experimental technique facilitates the non-intrusive measurement of the unsteady 3D temperature field of a premixed methane/air flame. The target flame visualization, which was achieved by the flame reaction of sodium in the supplied mists of sodium chloride solution and line-of-sight intensity images of the flame, was transformed into the temperature field using calibration with the sodium D-line reversal method combined with imaging from six CCD cameras located around the flame. The uncertainty in tomographic temperature measurement was confirmed for the steady axisymmetric flame under the influence of strong coflow. Tomographic temperature measurements were applied to the flickering flame with and without coflow, and the results were analyzed using proper orthogonal decomposition (POD) to understand the unsteady behavior of the temperature field of the flickering flame. The flickering energy was found to be dominant in the first two POD modes. Flame flickering with and without coflow was found to be dominant in the axisymmetric and non-axisymmetric modes, respectively. The characteristics of the flickering flame with and without coflow are discussed in this paper, based on spectrum analysis. The results suggest that the structure of the flickering flame is highly modified by the presence of even a small magnitude of coflow.

Keywords Temperature measurement · Tomographic reconstruction · Flame reaction · Premixed methane/air flame · Flickering · Co-flow · Flame structure · POD analysis

---

N. Fujisawa · T. Yamagata (✉)
Visualization Research Center, Niigata University,
8050 Nino-cho, Ikarashi, Nishi-ku, Niigata, 950-2181, Japan
e-mail: yamagata@eng.niigata-u.ac.jp

N. Fujisawa
e-mail: fujisawa@eng.niigata-u.ac.jp

J. Yamada
Graduate School of Science and Technology, Niigata University,
8050 Nino-cho, Ikarashi, Nishi-ku, Niigata, 950-2181, Japan

1 Introduction

The measurement of flame temperature has been a topic of interest in combustion engineering for many years. However, it has not been hitherto fully accomplished owing to the difficulty posed by the three-dimensional (3D) and unsteady nature of the flame. The existing experimental methods of flame temperature measurement are mostly point-wise techniques that involve the use of a thermocouple or resistance thermometer, which are practical but intrusive in nature. In the recent years, more reliable temperature measurement methods have been proposed using optical techniques such as laser-induced fluorescence, Rayleigh scattering, and Raman scattering [1, 2]. Although these techniques are expensive as they require high-power lasers and highly intensified image sensors, among others, a few less-expensive temperature measurement methods are available, namely, rainbow-schlieren deflectometry [3, 4], interferometry [5], and laser-speckle photography [6, 7]. These methods measure the density field created in the flame temperature field by using rather complex image analysis techniques. The option of measuring temperature using the two/three-color pyrometer is also available, which is non-intrusive but requires soot particles [8].

Flame temperature measurement using the flame reaction technique is becoming one of the powerful methods in the recent times because it can measure the entire temperature field of the flame non-intrusively, by assuming its axisymmetry [9]. This technique requires only a small amount of spray mists for flame visualization, using alkali metals such as sodium (Na), potassium (K), and lithium (Li) [10]. The spontaneous emissions of light from the metal atoms are so strong that flame images are well-detected by a standard CCD camera, thus eliminating the need for an image intensifier. The principle behind this technique is that the intensity of the light emitted from the flame visualized using flame reaction is a function of its temperature in reference to the Maxwell-Boltzmann statistics of thermodynamics. Later, the accuracy of the measured temperature can be improved by correcting the number density distribution of the metal atoms in the flame using measurement integrated analysis [11]. However, this technique is still limited to the measurement of axisymmetric flame temperature.

Computer tomography is a powerful experimental technique for measuring the 3D field of interest, from line-of-sight images captured by multiple cameras located around the target field of interest. To implement this, tomographic reconstruction techniques such as the algebraic reconstruction technique (ART) [12] and multiplicative algebraic reconstruction technique (MART) [13] have been adopted for analysis during the reconstruction of the 3D field of interest. The ART uses the deviation of the virtual projection from the measured projection, and iteratively optimizes the object coefficient in the algebraic equation, whereas the MART uses the multiplicative equation for optimization. Although the ART is often used in tomographic reconstruction, the MART retains a non-negative object field in the reconstruction, owing to which the reconstruction error is almost equal to that associated with the ART [14]. These techniques have been studied in literature and their applications to combustion engineering have been reported, such as flame temperature evaluation using density measurement [15], carbon monoxide measurement in laminar flames [16], chemiluminescence measurement in turbulent flames [17, 18], and flame temperature measurement using the two-color pyrometric technique [19].

Flame flickering is a fundamental phenomenon that occurs in a flame owing to Kelvin-Helmholtz instability in the shear layer between the flame and the surrounding air, under the influence of buoyancy forces [20–22]. The flickering frequency depends on the Froude number, which is the ratio of the inertia to the buoyancy forces of the flame. This frequency (10–20 Hz) is almost insensitive to experimental details such as the fuel type, flow rate, and burner size [23]. According to experimental studies, the dimensionless flickering frequency increases with the increase in Froude number, to the power of 0.5 [24, 25], whereas the flickering motion is known to be influenced by the coflow [11, 26–28]. The flickering frequency and oscillation amplitudes of flames under the influence of coflow were studied using the diffusion flame [27, 28] and premixed flame [11]. The experimental results indicate that the flickering amplitude of the flame decreases gradually with the increase in coflow velocity and increases with the increase in the equivalence ratio of the premixed flame [11]. Moreover, the results indicate that the flickering phenomenon is fully suppressed at strong coflow velocity [27, 28] by a mechanism believed to be caused by the reduction in the Kelvin Helmholtz instability in the shear layer between the flame and the surrounding air with an increase in coflow velocity. However, this mechanism of suppression has not yet been fully understood owing to the complex interaction between flame flickering and coflow.

The purpose of this paper is to describe instantaneous 3D temperature measurement using the flame reaction technique combined with tomographic reconstruction, applied to the premixed methane/air flame with and without coflow. Furthermore, snapshot proper orthogonal decomposition (POD) analysis is introduced in the measurement of the temperature field to understand the structural change in flame flickering due to the influence of coflow.

2 Experimental Apparatus and Method

2.1 Experimental setup

The experimental apparatus for studying the premixed methane/air flame is shown in Fig. 1. Methane and air are supplied as fuel gases from different containers to the straight-pipe

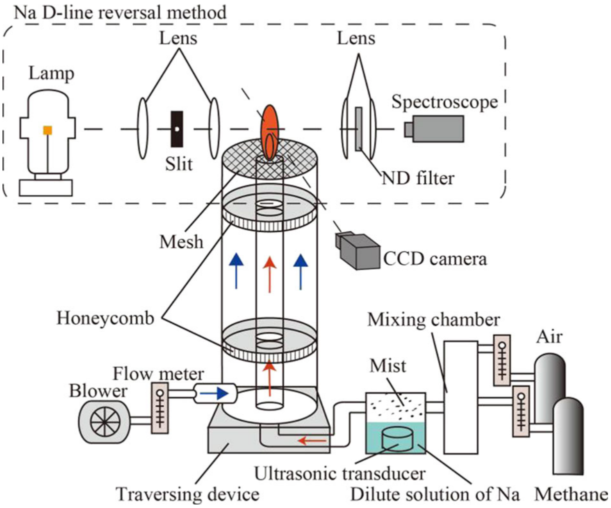

Fig. 1 Experimental setup for flame temperature measurement

burner of diameter $d = 24$ mm, through flow meters and a mixing chamber. The experiment was conducted in a calm-air environment with surrounding air temperature of ~ 293 K. The premixed methane/air flame was not visible at the equivalence ratio $\varphi < 2$, owing to the low emission intensity of the carbon-containing species in the flame of methane/air. The value of φ was adjusted by controlling the flow rates of methane and air independently. The total flow rate of the fuel was maintained at 6.1 l/min in this experiment. The flow through the coaxial pipe surrounding the burner provided the air coflow for controlling the flickering of the flame. The diameter of the coflow pipe was 154 mm. Honeycomb structures were installed inside the pipe to maintain a uniform coflow velocity, and a screen was placed at the exit of the fuel pipe to avoid flashback. The coflow velocity was estimated from the flow rate measured by the flow meter, and was controlled using the valve at the exit of the blower. The exit velocity of fuel flow was set to a constant 0.22 m/s and that of coflow was varied in the range 0–0.36 m/s, which corresponds to the coflow velocity ratio $U_r (= U_c/U_f) = 0\text{–}1.6$, where U_c and U_f represent the coflow and fuel velocities, respectively. The Froude number was fixed at $Fr\ (= U_f^2/gd) = 0.21$ in the present experiment.

2.2 Flame visualization

Flame visualization was conducted by supplying a mist of sodium chloride solution to the premixed fuel of methane/air. The mass weight of the mist was controlled by the DC voltage supplied to the ultrasound humidifier, which generated mist of approximately 1 μm in diameter. The sodium chloride solution used contained 0.5 mol/l of Na in water. The metal atoms of Na in the flame emitted light at a distinct spectrum with 589 nm wavelength. The net mass flow rate of the mist injected through the burner was 0.2 mg/s, which was measured by sampling it and measuring its net weight using a high-precision weight meter. The flame temperature did not change with the supply of mist, and this was confirmed during the experiment through flame temperature measurement using a thermocouple [9].

The visualized images of the flame were captured by six CCD cameras (SONY XC-HR57: 659 × 494 pixels with 8 bits) operating synchronously at 60 Hz, with electronic shutter speed of 250 Hz corresponding to an exposure time of 4 ms. These cameras were placed around the flame, equidistant at 360 mm from its center and normal to its axis. The cameras comprised lenses with focal length 16 mm and f-number 8, attached by a narrow band-pass filter (589 ± 3 nm) to remove background noise.

2.3 Evaluation of flame temperature field

The temperature field of the flame was evaluated by analyzing the images visualized using the flame reaction technique. According to Maxwell-Boltzmann statistics of thermodynamics [29], the inverse temperature $1/T$ can be expressed in terms of the intensity i of the visualized images, as follows:

$$1/T = a_1 \ln(i) + c_1 \tag{1}$$

where a_1 is a function of the wavelength of the emitted light and c_1, which depends on the experimental condition, is a function of the number density of the metal atoms. The value of a_1 for the metal atoms of Na was determined as -0.041, whereas c_1 can be determined from a calibration study on the true temperature and local intensity of the flame [9].The true temperature, in turn, can be determined using the Na D-line reversal method, by correcting the influence of the cool boundary layer around the flame

[30, 31]. The local intensity of the flame in Eq. 1 can be evaluated by measuring the line-of-sight intensity of a steady axisymmetric flame using Abel transformation. The assumption of uniform number density distribution of Na in the flame does not always hold good and hence, number density distribution was determined through measurement integrated analysis by numerically solving the transport equations of mass and momentum and the state equation (using the experimental temperature field under the assumption of uniform number density distribution of Na [10]). The boundary conditions were prescribed by the experimental data on fuel velocity and coflow velocity of air whereas Neumann conditions were applied to the outlet boundary. The iterative procedure described by Fujisawa et al. [11] was applied to measure the temperature. When measurement integrated analysis combined with the iterative procedure is introduced in the temperature calibration, a linear relationship between $1/T$ and the logarithmic intensity $\ln(i)$ is obtained, along with the constant $a_1(= -0.039)$ that agrees closely with its theoretical value $(a_1 = -0.041)$ for a temperature range of 1,700–2,000 K, thus validating the temperature correction approach [11].

2.4 Tomographic reconstruction

Figure 2 shows the top view of the experimental arrangement for the measurement of the instantaneous 3D temperature field of the flame. The observations were made by the six synchronously operating CCD cameras placed around the target flame at neighboring-camera angles of 30°. The target area is 80 mm and images were captured for 2 s so that the total number of images per CCD camera is 120. A narrow band-pass filter is attached to each camera to remove background noise, except in the case of the emission spectrum of Na at 589 nm. To avoid lens distortion of the image, the captured images were calibrated against a calibration plate comprising equidistant mesh lines at 5 mm intervals. The depth of focus of the camera lenses was estimated at 130 mm, which is much larger than the diameter of the flame.

The 3D intensity field of the flame was reconstructed from the flame images using the MART, which is one of the tomographic reconstruction algorithms [13, 14] offering the advantage of a non-negative object field for reconstructing non-negative scalars. The MART offers better convergence of the solution than that achieved using the ART with roughly the same reconstruction error, in this example. This technique undertakes the optimization task

Fig. 2 Top view of flame and imaging system

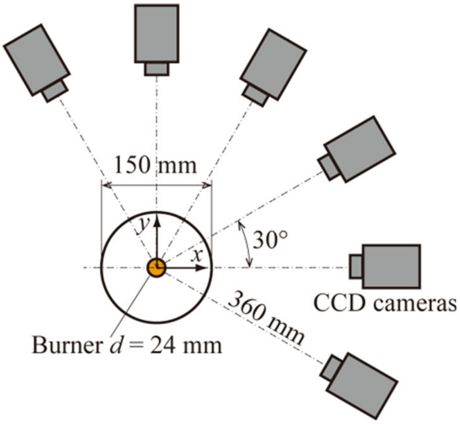

for the linear case, in which each basis function is defined by a single parameter. The object function to be reconstructed is given by

$$\bar{i}(x, y) = \sum_{i=1}^{M} A_i b(x - x_i, y - y_i) \tag{2}$$

where M is the total number of grids, b is the basis function approximated by the cubic B-spline function, and A_i is the coefficient of the i^{th} basis function. In this study, the number of grids was set to 81 × 81 × 139 in the x, y, and z directions, respectively, where x and y are the horizontal coordinates, and z is the vertical coordinate of the flame.

The MART uses a multiplicative correction factor C_i for obtaining the next step of the coefficient in the basis function:

$$A_i^{n+1} = C_i^n A_i^n \tag{3}$$

where

$$C_i^n = 1 - 0.5W_i^n(1 - I_i/\bar{I}_i) \ \text{ for } \ \bar{I} \neq 0, C_i^n = 1 \ \text{ for } \ \bar{I} = 0 \tag{4}$$

where n denotes the nth iteration and W_i is the weighting factor, which is set to 1 in this study.

2.5 POD analysis

POD is one of the statistical methods for analyzing the low-dimensional representation of the multidimensional flame temperature field. By using POD analysis, the most energetic structure of the flame can be extracted by decomposing the fluctuating properties of the temperature field into a linear sum of orthogonal eigenfunctions of temporal and spatial correlations. Snapshot POD [32] has been applied to turbulent flows to extract a coherent structure [33–36] whereas there are very few applications of POD analysis to the flame except for a study on flame velocity field by Duwig and Iudiciani [37].

Snapshot POD was introduced in the analysis of the 3D temperature field of the premixed methane/air flame in the present study. The basic principle of snapshot POD is that it yields a set of orthogonal eigenfunctions that are optimal in energy, representing temporal and spatial correlations of the instantaneous temperature field $T(x, t_k)$, which is acquired at time t_k, where $k = 1,2,\ldots N$. POD analysis was conducted over 120 snapshots of the 3D temperature field. The sufficiency of the number of snapshots was confirmed by the results obtained from the analysis of the reduced number of 60 snapshots. The reason for the need of fewer snapshots in this particular case is the dominant energy in the first two POD modes compared to the case of turbulent flows, which requires at least 500 snapshots [34–36]. POD analysis allows the evaluation of the mean temperature field in the 0^{th} POD mode T_0 and the fluctuating temperature field in the higher POD modes T_k. These modes are obtained by solving the following eigenvalue problem:

$$C_{jk}\boldsymbol{a} = \lambda_k \boldsymbol{a} \tag{5}$$

where C_{jk} is the two-point correlation matrix of the temperature field, given by

$$C^{jk} = \frac{1}{N} \int T(x, t_j) T(x, t_k) dx \qquad (j, k = 1, 2, \ldots .N) \tag{6}$$

Here, $\boldsymbol{a}$ is the eigenvector and λ_k is the eigenvalue of C_{jk} in the k^{th} mode. The eigenvectors and eigenvalues can be obtained by solving the above equations numerically.

A linear combination of $\boldsymbol{a}$ and T can be used to express T_k, as follows:

$$T_k(x) = \sum_{n=1}^{N} a_n^k T(x, t_k) \tag{7}$$

The dimensionless POD mode $\overline{T_k}$ was used in the present study. The 0^{th} POD mode $\overline{T_0}$ was made dimensionless using the maximum mean temperature and the k^{th} POD modes $\overline{T_k}$ ($k = 1, 2 \ldots N$), using the maximum fluctuating temperature. They were arranged in the order of the energy fraction in each POD mode. The fluctuating energy E_k of the corresponding POD mode is expressed by the eigenvalue λ_k divided by the total fluctuating energy E_t, as follows:

$$E_k = \frac{\lambda_k}{E_t} \tag{8}$$

where

$$E_t = \sum_{k=1}^{N} \lambda_k \tag{9}$$

3 Results and Discussions

3.1 Uncertainty in temperature measurement

Uncertainty in tomographic temperature measurement arises from the tomographic reconstruction error and the uncertainty in temperature evaluation using the flame reaction technique. The tomographic reconstruction error is evaluated by comparing the reconstructed and analytical intensity distribution values. In the present study, a CosGauss phantom function [13] was used as the reference intensity distribution. This function provides an asymmetric double-peak (as shown in Fig. 3) with adequate complexity to simulate the non-axisymmetric flame and evaluate the tomographic reconstruction error. It is the same function that was used for evaluating the tomographic reconstruction error [13, 14]. Using the CosGauss function, the intensity fields from various angles of observation were artificially generated and used as inputs for the tomographic reconstruction of the 3D intensity field. The generated images have a spatial resolution of 512 × 512 pixels, which is approximately the same as those of experimental images. The tomographic reconstruction

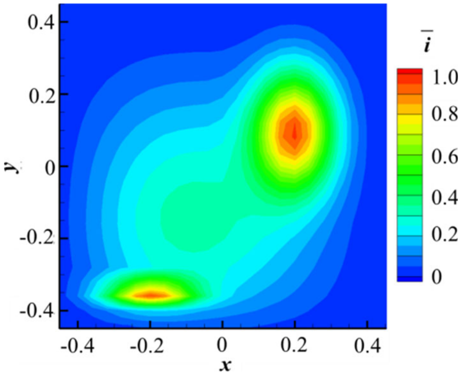

Fig. 3 Reference phantom field

error with respect to the reference intensity $\bar{i}$ was evaluated using the RMS error E_{rms}, which is defined as follows:

$$E_{rms} = \sqrt{\frac{\sum_{j=1}^{N}\left(i(x_j, y_j) - \bar{i}(x_j, y_j)\right)^2}{\sum_{j=1}^{N}\left(i(x_j, y_j) - \bar{i}_{av}\right)^2}} \tag{10}$$

where $\bar{i}_{av}$ is the average intensity of the phantom field.

Figure 4 shows the variations in the values of E_{rms} with respect to the number of cameras N_c for two cases, namely, flame reaction and speckle photography [14] (whose density field was reconstructed from the projected beam's deflection angle from the line integral of the density gradient). Error analysis for speckle photography was conducted in the case of cameras 3 and 5 by Ko and Kihm [14]. The present result indicates that the reconstruction error obtained using the flame reaction technique is smaller than that obtained from the density field using speckle photography. Hence, the density gradient had to be integrated along the line-of-sight direction to evaluate the density field in speckle photography whereas the evaluation of the intensity field using the flame reaction technique is a straightforward approach that does not require integration. This result suggests that temperature measurement using the flame reaction technique offers better accuracy than does speckle tomography. The result also indicates that the reconstruction error associated with the flame reaction technique decreases gradually with the increase in the number of cameras, similar to the case of speckle tomography. The value of E_{rms} was found to be 9.2 % in the present study, in which six CCD cameras were used whereas it is known to increase to up to 19.5 % when three CCD cameras are used.

The other error in temperature measurement arises during temperature evaluation, which consists of temperature calibration and image analysis, using the flame reaction technique. Uncertainties in temperature calibration using the flame reaction technique can be estimated at 30 K (with the sodium D-line reversal method), 10 K (owing to the scattering of calibration during flame reaction), 20 K (during non-uniform number density correction), and 30 K (with image analysis). The tomographic reconstruction error values were estimated at

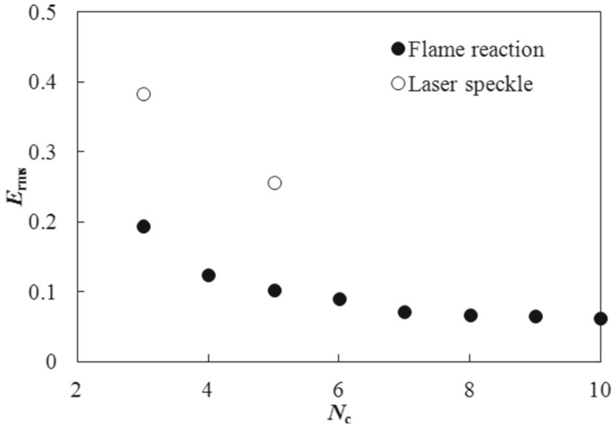

Fig. 4 E_{rms} versus N_c

30 and 60 K for six and three cameras, respectively, and consequently, the total uncertainties in temperature measurement were estimated at 64 and 82 K, respectively. This result suggests that tomographic reconstruction error is the major source of error in temperature measurement although other error sources cannot be neglected.

3.2 Tomographic temperature measurement in steady axisymmetric flame

To confirm the accuracy of tomographic temperature measurement, the temperature field reconstructed using the MART was compared with that obtained from Abel transformation for the steady axisymmetric flame under the influence of coflow at $U_r = 1.6$, which is adequately high for stabilizing the flame flickering [11]. The value of φ was set to 1. The validity of temperature measurement using Abel transformation has been confirmed by thermocouple measurement combined with the Na D-line reversal method [11]. Figure 5a shows an example of flame visualization using the flame reaction technique, in which the intensity contour of the flame was captured by one of the six CCD cameras. Figures 5b and c display the vertical cross-sections of the temperature fields of the flame, measured using tomographic reconstruction and Abel transformation, respectively. The two temperature fields are seen to agree closely with each other, and this confirms the validity of tomographic reconstruction conducted using the six cameras. Both temperature fields show a high temperature region near the burner exit owing to active chemical reaction in the flame, which is a well-known characteristic of the premixed flame at $\varphi = 1$ [9]. Radial resolution values of 81 and 242 grids were obtained using tomographic reconstruction and Abel transformation, respectively. The spatial resolution of 0.3 mm obtained using tomographic reconstruction was fine enough to resolve the flickering of the flame in the present experiment. Fewer grids were used in tomographic reconstruction to avoid the long computational time (approximately 100 times longer than that of Abel transformation).

3.3 Tomographic temperature measurement for flickering flame with and without coflow

Figure 6 shows the time variations in the instantaneous temperature field of the flickering flame at $\varphi = 1$ and $U_r = 0.6$, which were measured using the flame reaction

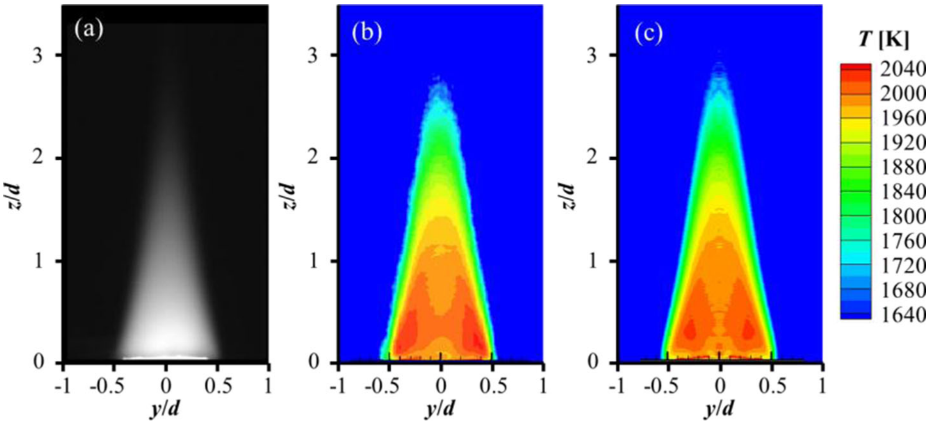

Fig. 5 Temperature field of premixed methane/air flame ($\varphi = 1$): **a** flame visualization, **b** temperature field obtained using tomographic reconstruction, **c** temperature field obtained using Abel transformation

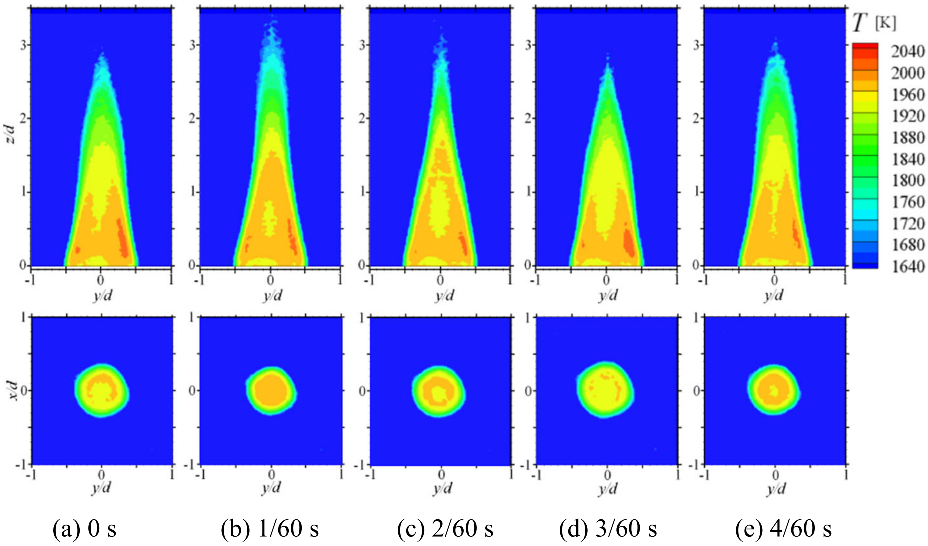

Fig. 6 Time variation in temperature field of flickering flame with coflow ($U_r = 0.6$)

technique combined with tomographic reconstruction. The results are shown for the vertical and horizontal temperature distributions through the flame axis at $z/d = 1$. The time interval between the sequential temperature fields is 1/60 s, which corresponds to the highest frame rate of the cameras. An observation of the flame flickering shows an increase in the flame height in phases (a)–(c) and decrease in the following phase (d), (e) which almost resembles the temperature contour of phase (a) owing to the periodicity of flame flickering. The flame height is observed to be the minimum in phases (d) and maximum in phase (b). In the phases of increasing flame height (a)–(c), the width of the flame decreases in its middle region, followed by its separation at its mid height (d). In phases (b) and (c), the width of the flame is seen to be narrowed due to its vertical stretching motion, followed by a sudden decrease in the flame height (d) owing to its separation. Therefore, flame flickering with weak coflow is characterized by the periodic oscillation of the flame at a frequency of approximately 15 Hz, which corresponds to the Strouhal number $St = 0.2$. The axisymmetry of this periodic oscillation of the flame is also found in the horizontal cross-section of the temperature field at $z/d = 1$, which is circular independent of the phase of the flickering flame but with periodic change in the flame diameter.

The corresponding temperature distributions in the vertical and horizontal cross-sections of flame flickering without coflow at $\varphi = 1$ are shown in Fig. 7. The time variation in the temperature field indicates that unsteady flame flickering occurs in the field particularly close to the top of the flame and that the flickering accompanies the unsteadiness in the periodic oscillation of the flame, which may be due to the turbulence in the shear layer between the flame and the surrounding air. This result also suggests that both flame flickering and turbulence in the flame are suppressed by the influence of coflow. Such a non-axisymmetric temperature field can be measured only using the tomographic technique, which allows instantaneous measurement of a 3D temperature field. Therefore, the present results reveal that the tomographic flame reaction technique serves as a powerful tool for quantifying the 3D temperature field of an unsteady non-axisymmetric flame.

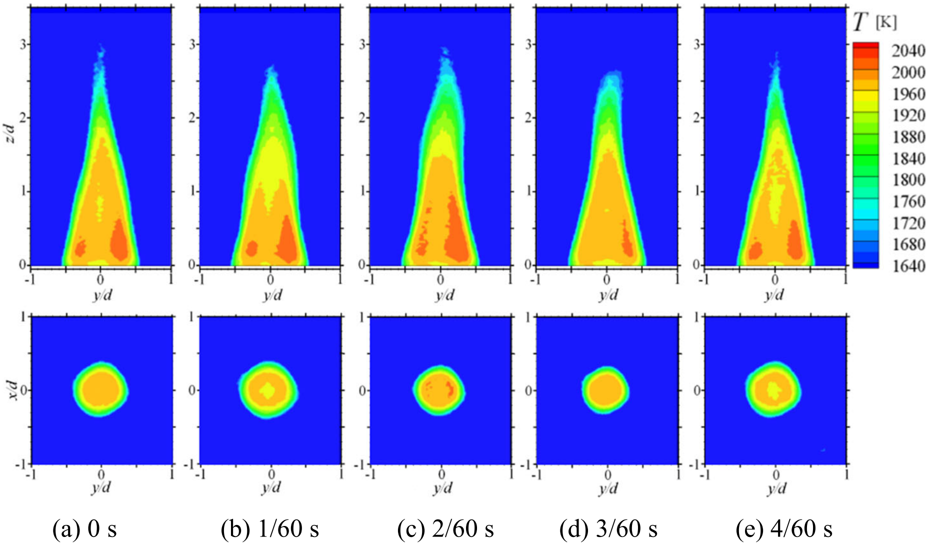

(a) 0 s (b) 1/60 s (c) 2/60 s (d) 3/60 s (e) 4/60 s

Fig. 7 Time variation in temperature field of flickering flame without coflow ($U_r = 0$)

3.4 POD modes of flickering flame with and without coflow

Figure 8 shows the POD modes of the vertical temperature fields of the periodically flickering flame at $\varphi = 1$ and $U_r = 0.6$. The modes were evaluated through POD analysis of 120 snapshots of the 3D temperature field of the flickering flame, which were obtained every 1/60 s. These POD modes do not vary significantly upon reducing the total number of snapshots to 60 because E_k dominates in the first two modes of the fluctuating temperature field [37]. The values of E_k in the 1st and 2nd POD modes were 38 % and 36 % of E_t, respectively, implying that 74% of E_k associated with the temperature arises from the first two POD modes. The 0th POD mode corresponded to the mean temperature field of the flame. The result agrees well with the mean flame temperature shown in Fig. 5, which confirms the validity of the present POD. The 0th POD mode showed the highest mean temperature near the burner exit and along the reaction front of the flame, which is a typical feature of the premixed flame at $\varphi = 1$ [9]. In contrast, the 1st POD mode showed the highest energy associated with fluctuating temperature near the top of the flame, along the shear layer at $z/d = 2$ and distributed symmetrically with respect to the flame axis. This result suggests that the temperature is highly fluctuating near the top of the flame whereas opposite correlation was observed in the lower shear layer at $z/d = 1$. Therefore, opposite temperature oscillations occur in the temperature field at the top of the flame and along the lower shear layer at z/d =1, although these oscillations are distributed axisymmetrically. In the 2nd POD mode, the temperature fluctuation was the highest along the shear layer, in the mid height of the flame at $z/d = 1$–2 whereas opposite correlation was observed near the top of the flame and at the burner exit, and the fluctuations are distributed axisymmetrically. Similarly, the axisymmetrical nature of the flame appeared in the 3rd to 5th POD modes, as seen in Figs. 8d–f, and the scale of the structure is seen to decrease with the increase in the mode number. The values of E_k in these POD modes are 3.2 %, 2.9 %, and 0.9 %, respectively. This indicates that the POD modes of a flickering flame with coflow are dominated by the axisymmetric modes of fluctuating temperature.

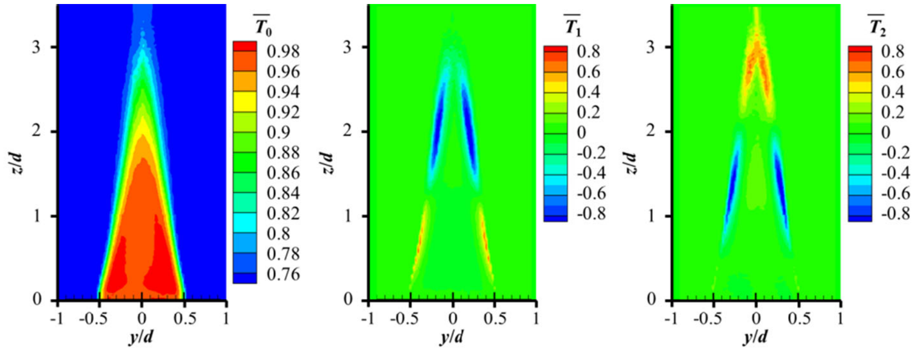

(a) 0th mode (b) 1st mode (c) 2nd mode

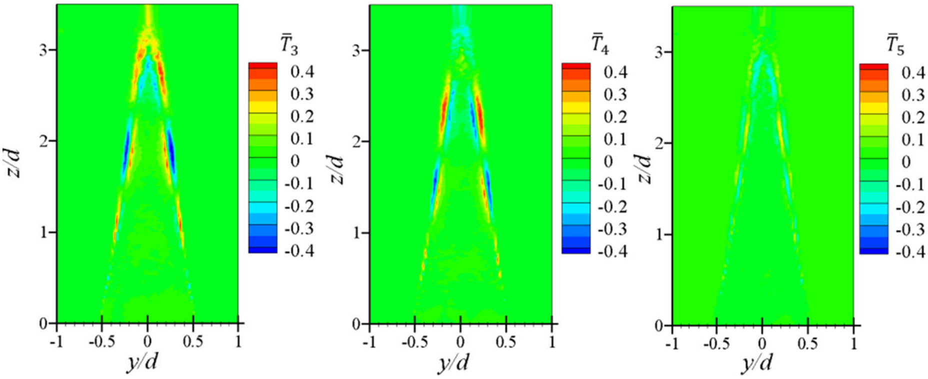

(d) 3rd mode (e) 4th mode (f) 5th mode

Fig. 8 POD modes of temperature field of flickering flame with coflow ($U_r = 0.6$)

Figure 9 shows the POD modes of the unsteady flickering flame without coflow at $\varphi = 1$. The mean temperature field of the 0th POD mode is in close agreement with that of the periodic flame flickering with coflow shown in Fig. 8. This indicates that the mean temperature field of the flame does not change significantly with coflow velocity. In contrast, the 1st and 2nd POD modes of the fluctuating temperature field are distributed non-axisymmetrically compared to those of the case with coflow (Fig. 8). High correlation in the first POD mode appeared along the right-hand-side of the shear layer in the flame at $z/d = 2$ whereas the weaker correlation was distributed along the left-hand-side of the shear layer at $z/d = 1.5$. In the second POD mode, high and low correlations occurred along the right and left shear layers, respectively, whereas the positions of the correlations were shifted along the shear layer compared to those in the first POD mode. The values of E_k in the 1st–5th POD modes were 36 %, 33 %, 5.6 %, 3.1 %, and 2.2 %, respectively, of E_t. These results indicate that the POD modes of the flickering flame without coflow were dominated by the non-axisymmetric oscillation of the flame. This behavior can be caused by the amplification of the unstable non-axisymmetric mode of Kelvin-Helmholtz instability in the shear layer along the flickering flame without coflow.

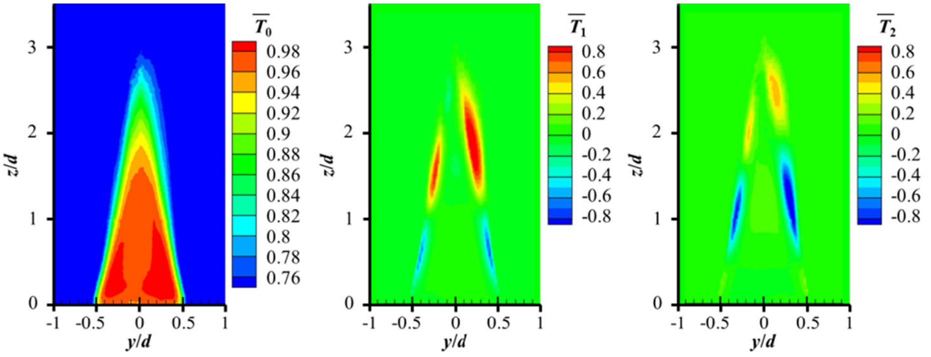

(a) 0th mode (b) 1st mode (c) 2nd mode

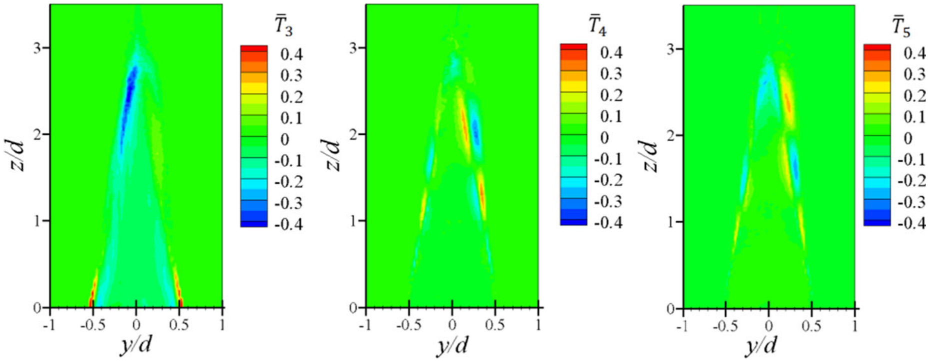

(d) 3rd mode (e) 4th mode (f) 5th mode

Fig. 9 POD modes of temperature field of flickering flame without coflow($U_r = 0$)

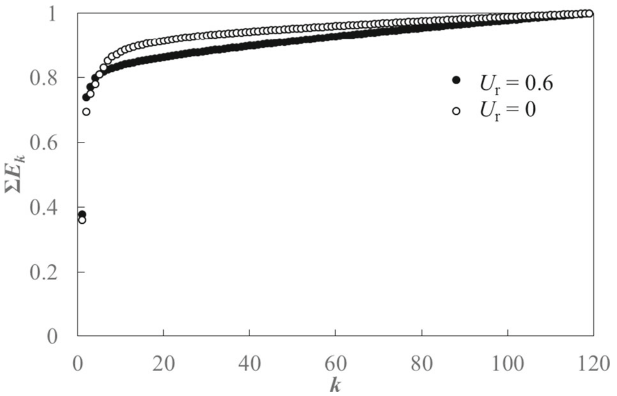

Fig. 10 Cumulative energy distributions of POD modes with and without coflow

Figure 10 shows the cumulative energy distributions of the POD modes of the flickering flame with and without coflow. The first two POD modes are observed to cover most of the E_k, independent of the presence of coflow. The cumulative energy values in the first two POD modes are higher in the case with coflow whereas most of the total cumulative energy distribution is higher in the case without coflow. This result indicates that the cumulative energy distribution gets suppressed by the coflow in the higher POD modes of the flickering flame, and this agrees with the behavior directly observed in the flame in Figs. 6 and 7.

3.5 Further analysis of unsteady behavior of flickering flame with and without coflow

Figures 11a and b show the power spectra of flame flickering with and without coflow, respectively. The spectrum of flame flickering with coflow shows a distinct peak at a frequency of 15 Hz whereas that without coflow shows a broad spectrum peak at 14 Hz. Thus, coflow causes an increase in the peak frequency of flame flickering and magnifies its peak spectrum. This implies that the periodic oscillation of the flame is magnified in the absence of coflow whereas the spectrum distribution becomes sharper under the influence of coflow. Thus, the unsteady flickering of the flame without coflow (in Fig. 7) may be caused by the broadened spectrum of flame flickering, as seen in the 1st and 2nd POD modes in Fig. 11a. In contrast, the power spectra were magnified in the 3rd–5th POD modes owing to coflow. The low frequency spectra in the 3rd and 4th modes were magnified, and the spectrum at

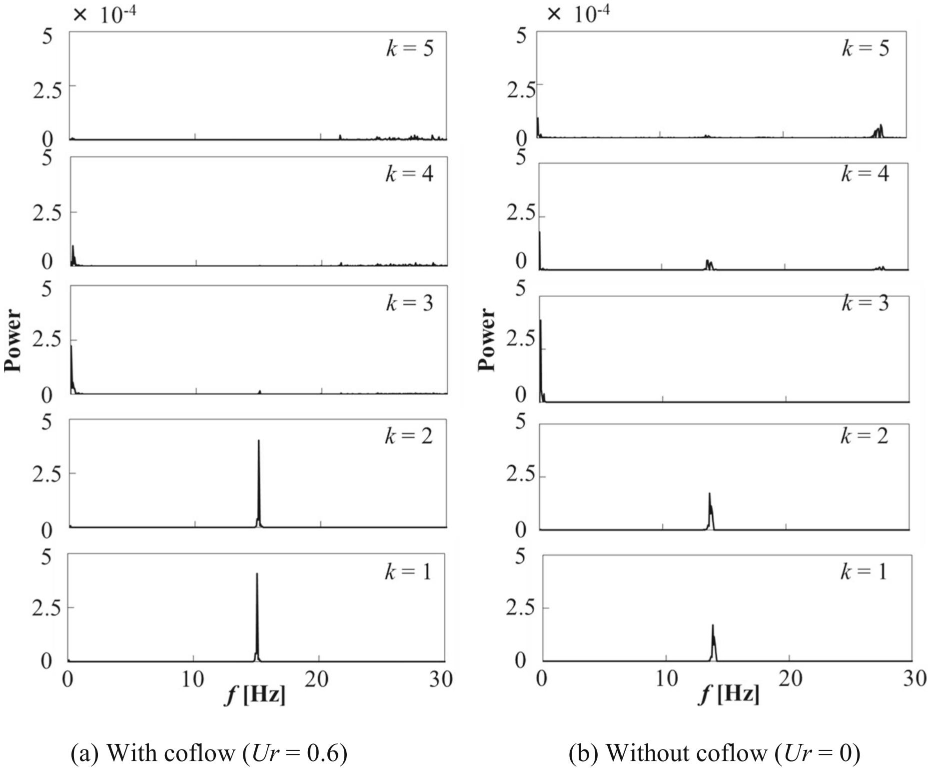

(a) With coflow ($Ur = 0.6$) (b) Without coflow ($Ur = 0$)

Fig. 11 Spectrum analysis of temperature fields with and without coflow the higher frequency range increased in the 5th POD mode. These results suggest that noisy spectra appear in the higher POD modes of the flickering flame without coflow, resulting in the unsteady oscillation of the flame, as seen in Figs. 6 and 7. The total cumulative energy associated with the flickering flame without coflow is observed to be 2.1 times higher than that with coflow, despite the lower peak spectrum of flame flickering.

4 Conclusions

An experimental technique for measuring the 3D flame temperature field using the flame reaction technique combined with tomographic reconstruction is described. This combined experimental technique facilitates the visualization of the 3D temperature field of a flickering flame with and without coflow. The flame visualization was conducted by supplying a mist of sodium chloride to a premixed methane/air flame at $\varphi = 1$, and the visualized images were captured by six CCD cameras located around the flame. The experimental method was validated for a steady axisymmetric flame at high U_r using Abel transformation. The 3D temperature measurement conducted for the flickering flame indicated that a flame is characterized by periodic flickering under weak coflow whereas without coflow, it demonstrates unsteady flickering. POD analysis of the flickering flame indicated that flame oscillation occurs in the first two POD modes of the fluctuating temperature field. The POD modes of the periodically flickering flame with coflow were found to be axisymmetric whereas those of the flame with unsteady flickering without coflow were non-axisymmetric. The spectrum analysis revealed that a sharp spectrum peak appears in the flame with coflow whereas the peak broadens and a noisy spectrum appears in the flame without coflow. Therefore, the structure of the flickering flame is significantly different in the cases with and without coflow, which in turn, is due to the elimination of the noisy spectrum in the higher POD modes of the flickering flame under the influence of coflow. The experimental results demonstrate that the tomographic flame reaction technique combined with POD analysis serves as a powerful tool for understanding the structure of the flickering flame, particularly that of the non-axisymmetrically flickering flame.

Acknowledgments The authors would like to express their thanks to Mr. T. Abe and Mr. H. Tomidokoro, graduate students of Niigata University, for their help during the course of this study.

References

1. Stricker, W.P.: Measurement of temperature in laboratory flames and practical devices. In: Kohse-Hoinghaus, K., Jeffries, J.B. (eds.) Applied Combustion Diagnostics. Taylor and Francis (2002)
2. Chung, S.H.: Several applications of laser diagnostics for visualization of combustion phenomena. J. Vis. **6**, 95–106 (2003)
3. Greenberg, P.S., Klimek, R.B., Buchele, D.R.: Quantitative rainbow schlieren deflectometry. Appl. Optics. **34**, 3810–3825 (1995)
4. Albers, B.W., Agrawal, A.K.: Schlieren analysis of an oscillating gas-jet diffusion flame. Combust. Flame **119**, 84–94 (1999)
5. Tieng, S.M., Lin, C.C., Wang, Y.C., Fujiwara, T.: Effect of composition distribution on holographic temperature measurement of a diffuse flame. Meas. Sci. Technol. **7**, 477–488 (1996)
6. Walsh, T.E., Kihm, K.D.: Tomographic deconvolution of laser Speckle photography applied for flame temperature measurement. In: Proceedings 7th Int. Symp. Flow Vis., pp. 898–903. Seattle (1995)
7. Fujisawa, N., Aiura, S., Ohkubo, M., Shimizu, T.: Temperature measurement of dilute hydrogen flame by digital laser-speckle technique. J. Vis. **12**, 57–64 (2009)

8. Panagiotou, T., Levendis, Y., Delichatsios, M.: Measurements of particle flame temperatures using three-color optical pyrometry. Combust. Flame **104**, 272–287 (1996)
9. Ohkubo, M., Nakagawa, Y., Yamagata, T., Fujisawa, N.: Quantitative visualization of temperature field in non-luminous flame by flame reaction technique. J. Vis. **14**, 101–108 (2012)
10. Ohkubo, M., Fujisawa, N., Nakamura, Y.: Visualization of temperature field in combustion by flame reaction technique. In: Proceedings 13th Int. Symp. Flow Vis., Nice, Paper 296 (2008)
11. Fujisawa, N., Abe, T., Yamagata, T., Tomidokoro, H.: Flickering characteristics and temperature field of premixed methane/air flame under the influence of co-flow. Energy Convers. Manage. **77**, 374–385 (2014)
12. Gordon, R.: A tutorial on ART (algebraic reconstruction techniques). IEEE Trans. **NS-21**, 78–92 (1974)
13. Verhoeven, D.: Limited data computed tomography algorithms for the physical sciences. Appl. Opt. **32**, 3736–3754 (1993)
14. Ko, H.S., Kihm, K.D.: An extended algebraic reconstruction technique (ART) for density-gradient projection: laser speckle phographic tomography. Exp. Fluids **27**, 542–550 (1999)
15. Schwarz, A.: Multi-tomographic flame analysis with a schlieren apparatus. Meas. Sci. Technol. **7**, 406–413 (1996)
16. Wondraczek, L., Khorsandi, A., Willer, U., Heide, G., Schade, W., Frischat, G.H.: Mid-infrared laser-tomographic imaging of carbon monoxide in laminar flames by difference frequency generation. Combust. Flame **138**, 30–39 (2004)
17. Ishino, Y., Ohiwa, N.: Three-dimensional computerized tomographic reconstruction of instantaneous distribution of chemiluminescence of a turbulent premixed flame. JSME Int. J. Series B **48**, 34–40 (2005)
18. Floyd, J., Kempf, A.M.: Computed tomography of chemiluminescence (CTC): high resolution and instantaneous 3-D measurements of a matrix burner. Proc. Combust. Inst. **33**, 751–758 (2011)
19. Hossain, M.M., Lu, G., Sun, D., Yan, Y.: Three-dimensional reconstruction of flame temperature and emissivity distribution using optical tomographic and two-color pyrometric techniques. Meas. Sci. Technol. **24**, 074010 (2013)
20. Buckmaster, J., Peters, N.: The infinite candle and its stability; a paradigm for flickering diffusion flames. In: 21st Int. Symp. Combust., pp. 1829–1836. The Combustion Institute, Pittsburgh (1986)
21. Katta, V.R., Roquemore, W.M.: Role of inner and outer structures in transitional jet diffusion flame. Combust. Flame **92**, 274–282 (1993)
22. Katta, V.R., Goss, L.P., Roquemore, W.M.: Effect of nonunity Lewis number and finite-rate chemistry on the dynamics of a hydrogen-air jet diffusion flame. Combust. Flame **96**, 60–74 (1994)
23. Huang, Y., Yan, Y., Lu, G., Reed, A.: On-line flickering measurement of gaseous flames by image processing and spectral analysis. Meas. Sci. Technol. **10**, 726–733 (1999)
24. Hamins, A., Yang, J.C., Kashiwagi, T.: An Experimental Investigation of the pulsation frequency of flames. In: 24th Symp. Combust (1992)
25. Sahu, K.B., Kundu, A., Ganguly, R., Datta, A.: Effects of fuel type and equivalence ratios on the flickering of triple flames. Combust. Flame **156**, 484–493 (2009)
26. Fujisawa, N., Nakashima, K.: Simultaneous measurement of three-dimensional flame contour and velocity field for characterizing the flickering motion of a dilute hydrogen flame. Meas. Sci. Technol. **18**, 2103–2100 (2007)
27. Gohari Darabkhani, H., Wang, Q., Chen, Q., Zhang, Y.: Impact of co-flow on buoyant diffusion flames flicker. Energy Convers. Manage. **52**, 2996–3003 (2011)
28. Wang, Q., Gohari Darabkhani, H., Chen, Q., Zhang, Y.: Vortex dynamics and structures of methane/air jet diffusion flames with air coflow. Exp. Therm. Fluid Sci. **37**, 84–90 (2012)
29. Bellac, M.L., Mortessagne, F., Batrouni, G.G.: Equilibrium and Non-Equilibrium Statistical Thermodynamics, pp. 267–334. Cambridge University Press, Cambridge (2004)
30. Thomas, D.L.: Problems in applying the line reversal method of temperature measurement to flames. Combust. Flame **12**, 541–549 (1968)
31. Philip, T., Bauman, L., Benton, R.: Sodium Reversal Plasma Temperature Measurement System. FE-15601, Topical Report (1992)
32. Sirovich, L.: Turbulence and the dynamics of coherent structures; part 1 coherent structures. Q. Appl. Math. **45**, 561–571 (1987)
33. Berkooz, G., Holmes, P., Lumley, J.L.: The proper orthogonal decomposition in the analysis of turbulent flows. Annu. Rev. Fluid Mech. **25**, 539–575 (1993)
34. Liu, Z.-C., Adrian, R.J., Hanratty, T.J.: Large-scale modes of turbulent channel flow: transport and structure. J. Fluid Mech. **448**, 53–80 (2001)

35. van Oudheusden, B.W., Scarano, F., van Hinsberg, N.P., Watt, D.W.: Phase-resolved characteristics of vortex shedding in the near wake of a square-section cylinder at incidence. Exp. Fluids **39**, 86–98 (2005)
36. Muld, T.W., Efraimsson, G., Henningson, D.S.: Mode decomposition on surface-mounted cube. Flow Turbul. Combust. **88**, 279–310 (2012)
37. Duwig, C., Iudiciani, P.: Extended proper orthogonal decomposition for analysis of unsteady flames. Flow Turbul. Combust. **84**, 25–47 (2010)